

The Evolution of Photospheric Current Density During an X9.3-Class Solar Flare

Hai-Li Li^{1,2}, Hong-Fei Liang¹, Xin-Ping Zhou³, Yu Liu⁴, Ni Meng¹, and Yu-Long Feng¹

Department of Physics, Yunnan Normal University, Kunming 650500, China; lhf@ynao.ac.cn

State Key Laboratory of Space Weather, Chinese Academy of Sciences, Beijing 100190, China

College of Physics and Electronic Engineering, Sichuan Normal University, Chengdu 610068, China; xpzhou@sicnu.edu.cn

School of Physical Science and Technology, Southwest Jiaotong University, Chengdu 610068, China

Received 2024 May 28; revised 2024 August 9; accepted 2024 August 15; published 2024 October 9

Abstract

This paper deduced the temporal evolution of the magnetic field through a series of high-resolution vector magnetograms and calculated the fine distribution map of current density during an X9.3-class flare eruptions using Ampère's law. The results show that a pair of conjugate current ribbons exist on both sides of the magnetic neutral line in this active region, and these conjugate current ribbons persist before, during, and after the flare. It was observed that the X9.3-class flare brightened in the form of a bright core and evolved into a double-ribbon flare over time. Importantly, the position of the double-ribbon flare matches the position of the current ribbons with high accuracy, and their morphologies are very similar. By investigating the complexity of current density and flare morphology, we discovered a potential connection between the eruption of major flares and the characteristics of current density.

Key words: Sun: activity – Sun: magnetic fields – Sun: flares – methods: data analysis

1. Introduction

Solar flares are high-energy eruptions that occur in the atmosphere of the Sun, often accompanied by coronal mass ejections (CMEs) (Gosling et al. 1991). Understanding and ultimately predicting intense explosive events such as large flares and CMEs are currently the cornerstones of solar research due to their socio-economic and environmental impacts (Simpson 2011; Vanselow 2020).

Research indicates that magnetic flux emergence and cancellation, sunspot rotation, and shear motion are three primary mechanisms triggering major flare eruptions (Raphaldini et al. 2023). In recent years, the quality and frequency of observations have significantly improved, largely due to the availability of data from the Solar Dynamics Observatory (SDO) and other satellites (Raboonik et al. 2016). One approach that has been explored is to investigate the local physical properties near Active Regions (ARs), such as magnetic flux (Metcalf et al. 2005; Regnier & Priest 2007), plasma velocity fields (Attié et al. 2018), magnetic helicity (Pariat et al. 2005), magnetic topology (MacTaggart et al. 2021), and magnetic twist (Kusano et al. 2020). Several evaluations of various predictive skills and their potential operational applications can be found in a series of papers (Barnes et al. 2016; Park et al. 2020).

Many studies have confirmed that currents may exist before a flare eruption and play a crucial role during the flare eruption process. Additionally, there is a close association between current ribbons in ARs and flare ribbons. A study by Lin (2000) found that the stronger the non-potentiality of ARs, the more

free magnetic energy is stored, leading to a higher probability of flare occurrence. Wang et al. (1994) found in their study of five X-class flares that the magnetic field shear along the magnetic neutral line (MNL) significantly increased after the flares. Ravindra et al. (2011) based on high-resolution observations of vector magnetic maps indicate the presence of a large amount of net electric current in ARs with strong shear along the main MNL. The study by Janvier et al. (2014) reveals that ARs capable of driving CMEs and flares exhibit a significant amount of net electric current. During the evolution of flares, changes in the morphology of flare ribbons may be related to current ribbons. Therefore, calculating the distribution of electric currents in strong magnetic fields on both sides of the MNL in ARs is of great importance for predicting the location and morphology of flare eruptions.

AR 12673 and its eruptions have been extensively studied (Yang et al. 2017; Chertok et al. 2018; Hou et al. 2018; Morosan et al. 2019). The AR first appeared at the end of August and started growing on September 3, rapidly strengthening its magnetic energy and helicity (Vasantharaju et al. 2019). Throughout its evolution, AR 12673 produced multiple X-class flares, C-class flares and M-class flares (Yamasaki et al. 2021). Among these flares, the X9.3 flare stands out as the largest recorded solar flare in Solar Cycle 24. It not only emitted intense white-light radiation but also generated gammaray emission (Lysenko et al. 2019). Moreover, it resulted in a geoeffective CME (Scolini et al. 2020). Additionally, an X2.2 flare was observed approximately 3 hr before the X9.3 flare

(Mitra et al. 2018), indicating a sequence of successive X-class flares from this AR. These bursts of accelerated high-energy particles have had significant space weather effects on Earth (Berdermann et al. 2018; Redmon et al. 2018).

This paper aims to deduce the temporal evolution of the magnetic field of AR 12673 using a series of high-resolution vector magnetograms. Based on the observed vector magnetic field, we calculated the current density distribution using Ampère's law. Finally, we investigated the correspondence between the extreme values of current density in the computed results and the positions and morphology of flare ribbons. The paper is organized as follows: First, the data processing and the method are discussed in Section 2, and then the results are given in Section 3. A discussion is presented in Section 4.

2. Calculation of Current Density

Research indicates the presence of spatially localized, highdensity sheet-like current structures within ARs (Savage et al. 2010). Extensive observational data on these structures have been obtained, particularly during periods of flare eruptions. However, accurately measuring the current intensity within these structures and characterizing the specific distribution of current density remain challenging. By measuring the polarized signals from the solar flare region, it is possible to invert a relatively accurate vector magnetic field. With the vector magnetic map, it becomes feasible to compute the distribution of current density using the differential form of Ampère's law. We calculate the current density, j_z , on the solar photosphere using the vector data B_t obtained from the helioseismology and magnetograph instrument. Due to the discrete nature of vector magnetic field data (Krall et al. 1982; Melrose 1991), the Ampère's law (Wilkinson et al. 1992; Canfield et al. 1993) in differential form is commonly expressed as

$$(j_z)_{i,j} = \frac{1}{\mu_0} \left(\frac{\partial B_y}{\partial x} - \frac{\partial B_x}{\partial y} \right)_{i,j},\tag{1}$$

where j_z represents the current density in the z-direction, μ_0 is the vacuum permeability, and B_x and B_y are the components of the magnetic field in the x and y directions, respectively. We calculate the values at the midpoints $A(x + \Delta x, y)$, $B(x, y + \Delta y)$, $C(x - \Delta x, y)$, and $D(x, y - \Delta y)$ along the four edges of the smallest square in Figure 1. The differential equation is modified as

$$(j_{z0})_{i,j} \approx \frac{1}{\mu_0} \left(\frac{(B_y)_{i+1,j} - (B_y)_{i-1,j}}{2\Delta x} - \frac{(B_x)_{i,j+1} - (B_x)_{i,j-1}}{2\Delta y} \right).$$
 (2)

This example illustrates that as the spatial resolution increases, i.e., the spatial grid widths $(\Delta x \text{ and } \Delta y)$ decrease, the computed current structures become finer.

Due to the influence of random noise, the actual measured magnetic field B'_t often incurs an error vector δB , where B_t represents the true value of the magnetic field within the AR

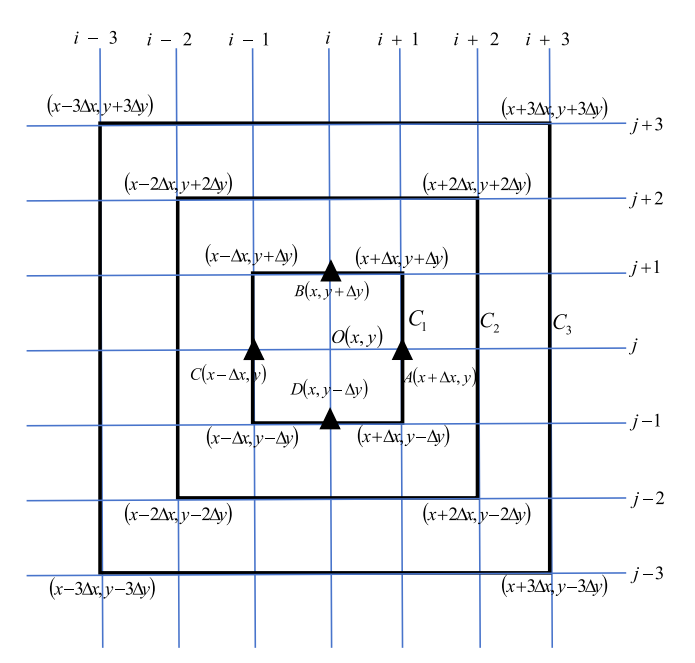


Figure 1. The integration paths of the Ampere's law integral form: the smallest square is the integration path C_1 , from the inside to the outside, the second square is the integration path C_2 , and the third square is the integration path C_3 . The four "triangle" points which are located in C_1 correspond to the differential form of Ampere's law. That is, based on the value of transverse magnetic field B_t at $A[x + \Delta x, y]$, $B[x, y + \Delta y]$, $C[x - \Delta x, y]$, and $D[x, y - \Delta y]$, the electric current density value at [x, y] can be calculated using the differential form of Ampere's law.

plus the systematic error. The actual measured magnetic field can be represented as $B'_t = B_t + \delta B$. The calculated current density j'_z is the sum of the true current density j_{z0} and the error current density δj_{z0} generated by random noise, namely

$$j'_{z0} = \frac{1}{\mu_0} \left(\frac{\Delta B_y}{\Delta x} - \frac{\Delta B_x}{\Delta y} \right) + \frac{1}{\mu_0} \left(\frac{\Delta \delta B_y}{\Delta x} - \frac{\Delta \delta B_x}{\Delta y} \right) = j_{z0} + \delta j_{z0}.$$
 (3)

When the random noise δB_x and δB_y remain constant, the decrease in Δx and Δy with increasing spatial resolution ultimately leads to an increase in error current density and obscures the true current density. Therefore, we typically use the integral form of Ampère's law

$$j_z = \frac{1}{\mu_0} \oint_l \mathbf{B}_t \cdot d\mathbf{l}/ds,\tag{4}$$

to calculate the current density. As shown in Figure 1, the loop integration method utilizes the values of the transverse magnetic field B_t along the integration path to calculate the average current density within the area enclosed by the integration loop, thereby obtaining the current density at the center O(x, y) of the integration loop. The resulting current density represents the average current density over the integration region. The integration path follows a

counterclockwise direction, and the integration loop centered at O(x, y) gradually increases in size (or moves from inside to outside) and is successively referred to as the small loop (a square with side length of $2\Delta x$, with integration path C_1), medium loop (a square with side length of $4\Delta x$, with integration path C_2), and large loop (a square with side length of $6\Delta x$, with integration path C_3). Among them, the integration path of the small loop follows the edges of a square at points $(x + \Delta x, y + \Delta y)$, $(x - \Delta x, y + \Delta y)$, $(x - \Delta x, y - \Delta y)$, and $(x + \Delta x, y - \Delta y)$, denoted as path C_1 , with the corresponding current density denoted as j_{z_1} . According to Equation (4), the calculation formula for the small loop is (where $ds = 2\Delta x 2\Delta y$):

$$(j_{z1})_{i,j} = \frac{1}{\mu_0} \oint_{C_1} \mathbf{B}_t \cdot d\mathbf{l}/ds$$

$$\approx \frac{1}{4\mu_0 \Delta x \Delta y} \sum_{n=i}^{i+1} \frac{(B_x)_{n-1,j-1} + (B_x)_{n,j-1}}{2} \Delta x$$

$$+ \sum_{n=j}^{j+1} \frac{(B_y)_{i+1,n-1} + (B_y)_{i+1,n}}{2} \Delta y$$

$$- \sum_{n=i}^{i+1} \frac{(B_x)_{n-1,j+1} + (B_x)_{n,j+1}}{2} \Delta x$$

$$- \sum_{n=i}^{j+1} \frac{(B_y)_{i-1,n-1} + (B_y)_{i-1,n}}{2} \Delta y.$$
(5)

The integration path of the medium loop follows the edges of a square at points $(x + 2\Delta x, y + 2\Delta y)$, $(x - 2\Delta x, y + 2\Delta y)$, $(x - 2\Delta x, y - 2\Delta y)$, and $(x + 2\Delta x, y - 2\Delta y)$, denoted as path C_2 , with the corresponding current density denoted as j_{z2} . According to Equation (4), the calculation formula for the medium loop is (where $ds = 4\Delta x 4\Delta y$):

$$(j_{z2})_{i,j} = \frac{1}{\mu_0} \oint_{C2} \mathbf{B}_t \cdot d\mathbf{l}/ds$$

$$\approx \frac{1}{16\mu_0 \Delta x \Delta y} \sum_{n=i-1}^{i+2} \frac{(B_x)_{n-1,j-2} + (B_x)_{n,j-2}}{2} \Delta x$$

$$+ \sum_{n=j-1}^{j+2} \frac{(B_y)_{i+2,n-1} + (B_y)_{i+2,n}}{2} \Delta y$$

$$- \sum_{n=i-1}^{i+2} \frac{(B_x)_{n-1,j+2} + (B_x)_{n,j+2}}{2} \Delta x$$

$$- \sum_{n=i-1}^{j+2} \frac{(B_y)_{i-2,n-1} + (B_y)_{i-2,n}}{2} \Delta y.$$
(6)

The integration path of the big loop follows the edges of a square at points $(x + 3\Delta x, y + 3\Delta y)$, $(x - 3\Delta x, y + 3\Delta y)$, $(x - 3\Delta x, y - 3\Delta y)$, and $(x + 3\Delta x, y - 3\Delta y)$, denoted as path C_3 , with the corresponding current density denoted as j_{z3} . According to Equation (4), the calculation formula for the

medium loop is (where $ds = 6\Delta x 6\Delta y$):

$$(j_{z3})_{i,j} = \frac{1}{\mu_0} \oint_{C3} \mathbf{B}_t \cdot d\mathbf{l}/ds$$

$$\approx \frac{1}{36\mu_0 \Delta x \Delta y} \sum_{n=i-2}^{i+3} \frac{(B_x)_{n-1,j-3} + (B_x)_{n,j-3}}{2} \Delta x$$

$$+ \sum_{n=j-2}^{j+3} \frac{(B_y)_{i+3,n-1} + (B_y)_{i+3,n}}{2} \Delta y$$

$$- \sum_{n=i-2}^{i+3} \frac{(B_x)_{n-1,j+3} + (B_x)_{n,j+3}}{2} \Delta x$$

$$- \sum_{n=i-2}^{j+3} \frac{(B_y)_{i-3,n-1} + (B_y)_{i-3,n}}{2} \Delta y. \tag{7}$$

Due to the inevitable presence of random noise in the measured vector magnetic field, appropriately expanding the integration path helps to reduce the impact of noise. However, this also reduces the resolution, preventing some fine current structures from being represented. Considering these factors, we selected the C_2 integration path, which provides a balanced result, for calculating the current density. This significantly enhances the reliability of current density calculations, facilitating our study of the relationship between solar flare eruptions and current density evolution.

3. SOLAR AR 12673

3.1. Observations and Data

In order to analyze a solar AR, we utilized a series of highresolution vector magnetograms to deduce the temporal evolution of the magnetic field of AR 12673 and calculated a detailed distribution map of the current density within the AR. In this section we describe the data set we used.

The SDO satellite's Helioseismic and Magnetic Imager (HMI) extensively observed AR 12673 (Pesnell et al. 2012), typically generating six wavelength-filtered images at the Fe I 617.3 nm spectral line, covering six polarization states. From these filtered images, images of the Stokes parameters I, Q, U, and V were derived, and they were inverted into magnetic field vector components using the Very Fast inversion code of the Stokes algorithm (Borrero et al. 2011). The atmospheric imaging component data used in this study include the 170 nm and 30.4 nm bands, where the 170 nm band covers the temperature minimum region and the photosphere, while the 30.4 nm band covers the chromosphere and transition region. To address the 180° azimuthal field ambiguity, we employed the "minimum energy" method (Leka et al. 2009). Additionally, we corrected a nearly 180° ambiguity in the transverse magnetic field vector direction (Welsch et al. 2013).

3.2. Result

Solar ARs are often characterized by the scale-dependent formation of energetic and localized magnetic structures (Abramenko et al. 1998). To analyze the solar AR, we utilized a series of high-resolution vector magnetograms to deduce the temporal evolution of the magnetic field of AR 12673. A continuous data set spanning 4 days prior to the solar flare eruptions with a 12 minute cadence enabled detailed examination of the long-term, gradual evolution, as well as the rapid changes during an X-class flare. Meanwhile, through measurements of the magnetic field vectors, we can compute the vertical component of the current density J_z , as shown in Figure 3, corresponding to the same times as depicted in Figure 2. We estimate the vertical component $J_z(x, y)$ using the photospheric magnetic field vectors B(x, y). The measurements of the magnetic field component intensities for AR 12673 on 2017 September 2 (column a), 2017 September 3 (column b), 2017 September 4 (column c), and 2017 September 5 (column d) are shown in the Figure 2.

The position of the sunspot umbra is marked with pink crosses, and the magnetic field is predominantly distributed to the east of the sunspot umbra. As time progresses, the magnetic field structure becomes increasingly complex. The computed current density, as shown in Figure 3, presents the current distribution every 4 hr. The morphology of the current evolves in response to the magnetic field evolution of the AR. On September 2nd, the AR appears relatively clear (see panels (a1)-(a6) in the figure), but starting from 12:00 UT on September 3rd (see panel (b4)), dispersed current structures begin to emerge in the main area of the AR. On September 5th, the dispersed current structures begin to converge and form complete ribbon-like structures. This indicates that there was already current present within the AR before the flare eruption. Moreover, as we approach September 6th, the current structure within the AR becomes increasingly complex. It should be noted that, due to the inability to measure the complete current density vector with available two-dimensional magnetic field measurements, in this work, we will assume that they are good approximations of the corresponding complete quantities (Jing et al. 2012).

Four days prior to the solar flare eruption, currents were already present within the AR and evolving over time. Dispersed current density began to appear on September 3 and continued to evolve over time. To understand the changes in current density on the day of the X9.3-class solar flare eruption, we used high-resolution vector magnetic maps to study the evolution of the magnetic field on 2017 September 6. Additionally, we employed the method described in Section 2 to calculate the fine distribution of current density on that day. As shown in Figure 4, we present line-of-sight (LOS) magnetograms (a1–a4), vector magnetograms (b1–b4), and current density distribution maps (c1–c4). The closer the

magnetic field structure is to the time of the flare eruption, the more complex it becomes.

However, we are aware that LOS magnetograms are subject to observational effects, and depending on the chosen viewing direction, they may vary. So, what exactly is the relationship between the eruption of solar flares and the magnetic field? To address this question, we utilized measured vector magnetograms to compute the current density distribution within the AR. Figure 4(b) depicts the vector magnetogram measured by SDO/HMI, with the grayscale identical to that of Figure 4(a), indicating the magnitude of the LOS magnetic field. The overlaid arrows on the grayscale image represent the strength of the transverse magnetic field, with the direction of the arrows indicating the orientation of the magnetic field and their length representing the magnitude of the magnetic field strength. To facilitate a clearer view of the structure of the vector magnetic field, blue arrows mean the transverse magnetic field of positive polarity regions, while red arrows signify that of negative polarity regions. Based on the vector magnetic field distribution shown in Figure 4(b), we computed the current density distribution within the AR, as illustrated in Figure 4(c). It can be observed that compared to the morphology of the AR and the distribution of vector magnetograms, the structure of the current is relatively simpler.

From the current density distribution maps (see Figure 4(c1) –(c4)), it is evident that there exist pairs of oppositely polarized current bands within the AR, which we refer to as "conjugate current bands." These conjugate current bands exhibit minor fluctuations during the period from 00:00 UT to 8:00 UT, with no significant changes. However, the considerable change in the current morphology at the moment depicted in Figure 4(c4) compared to the preceding current density map is noteworthy. As mentioned earlier, this time corresponds to the eruption of the X9.3-class solar flare at 12:00 UT. For a detailed analysis, we examine current density distribution maps taken at intervals of 12 minutes (see Figure 5).

Figure 5 depicts the computed current density during the period from 11:24 UT to 12:24 UT. Similar to Figure 4, a pair of elongated conjugate current bands with a "sandwich" structure is observed. The main positions of these current bands are indicated by black rectangles in the figure. We notice that in panels (a)–(c), the structure of the current bands remains largely unchanged. However, in panel (d), it can be observed that the negative polarity current band has been torn into several regions of high current density (depicted by deep blue small current islands), with some residual current remaining at the tearing sites. The tail of the positive polarity current band is also torn and directly disconnected. To verify the specific changes in current density, we subtracted the adjacent moments to obtain the current density running-difference images in Figure 6. This further confirms the significant variations in current density during the X9.3-class solar flare eruption (see Figure 6(d) and (e)).

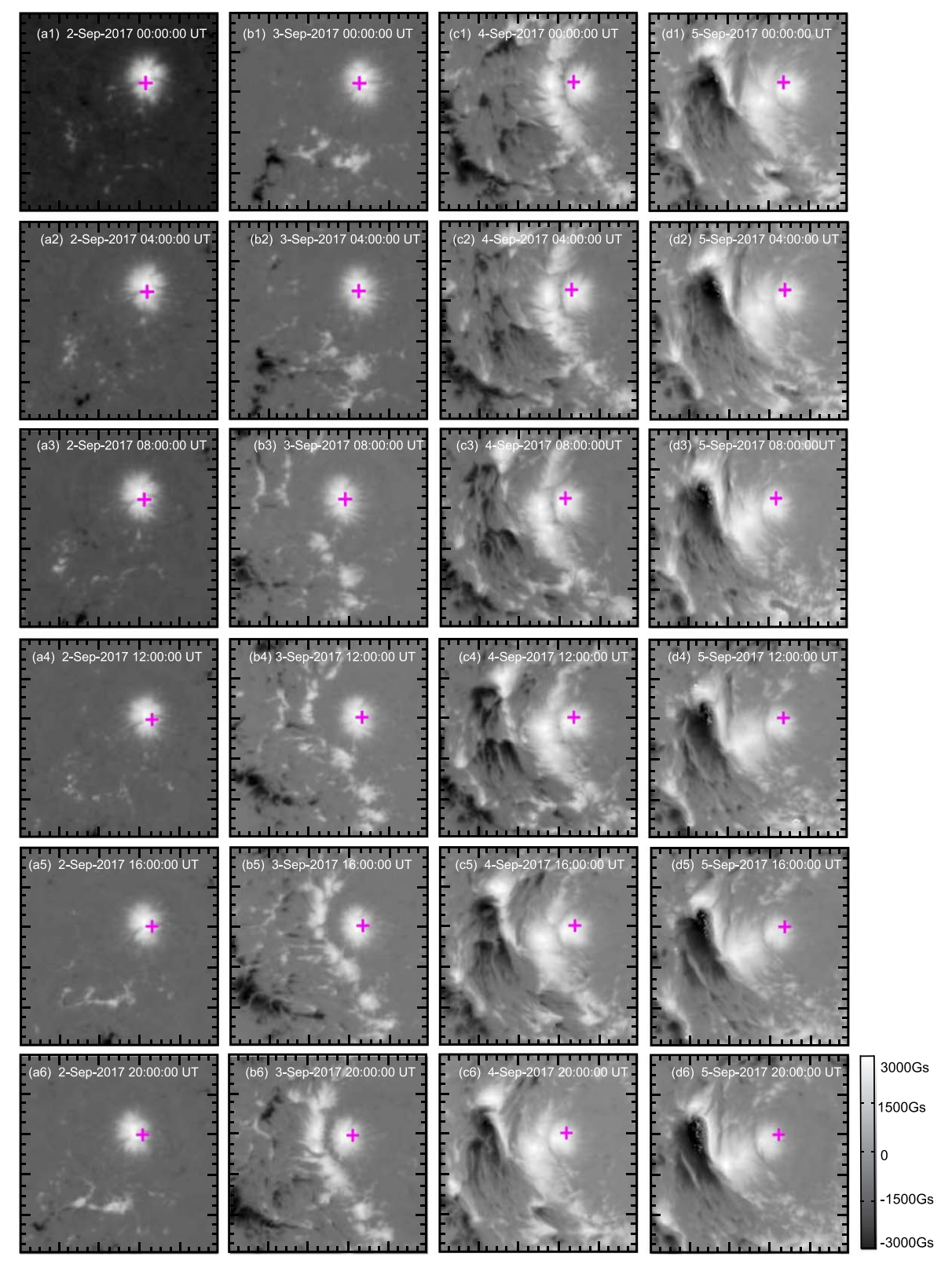


Figure 2. LOS magnetograms of AR 12673, measured on 2017 September 2 (column a), 2017 September 3 (column b), 2017 September 4 (column c), and 2017 September 5 (column d). The pink "+" symbol indicates the center of the sunspot umbra.

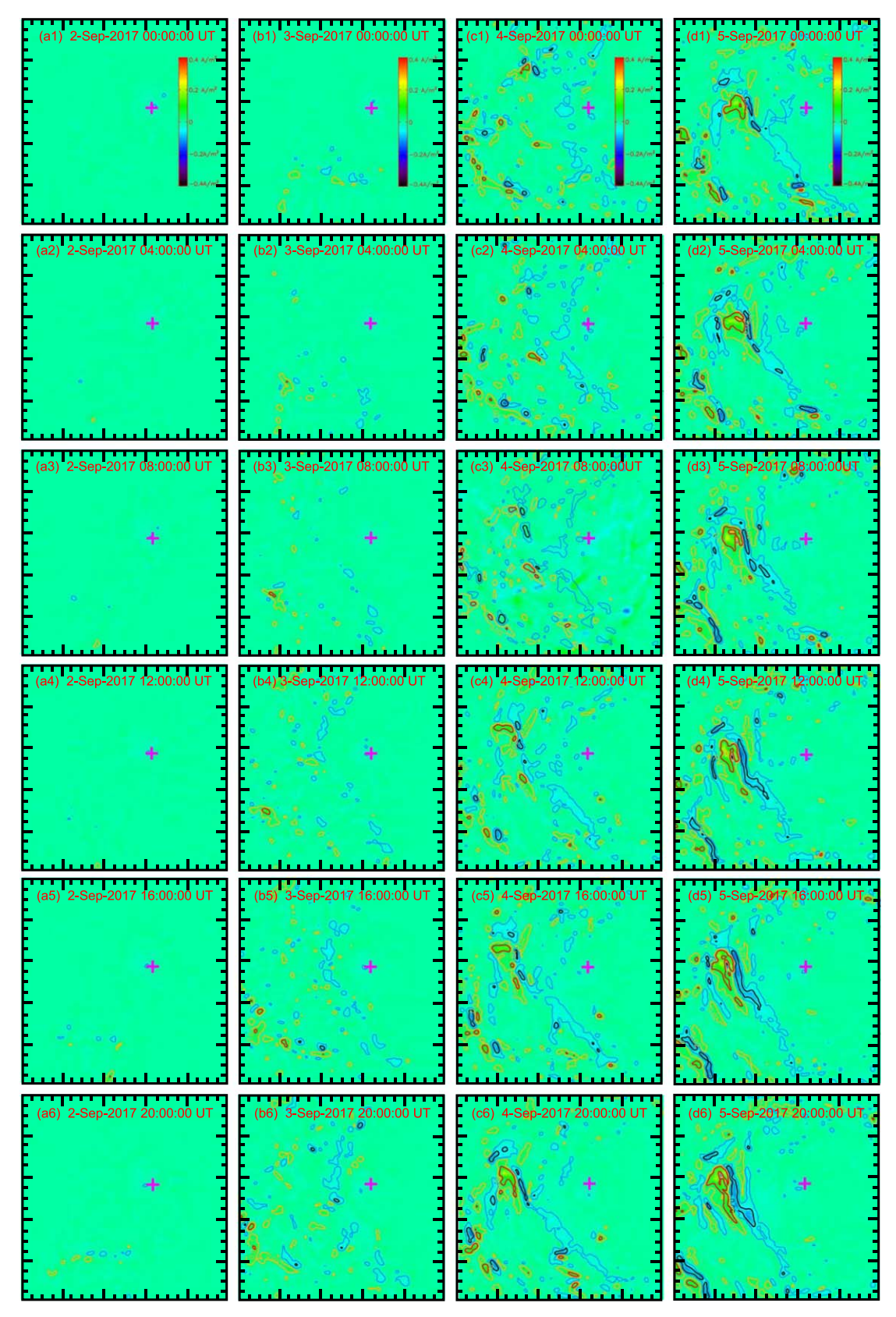


Figure 3. Current density distribution maps of the AR on 2017 September 2 (column a), 2017 September 3 (column b), 2017 September 4 (column c), and 2017 September 5 (column d), with the color bar on the right representing the current density and the pink "+" symbol marking the center of the sunspot umbra.

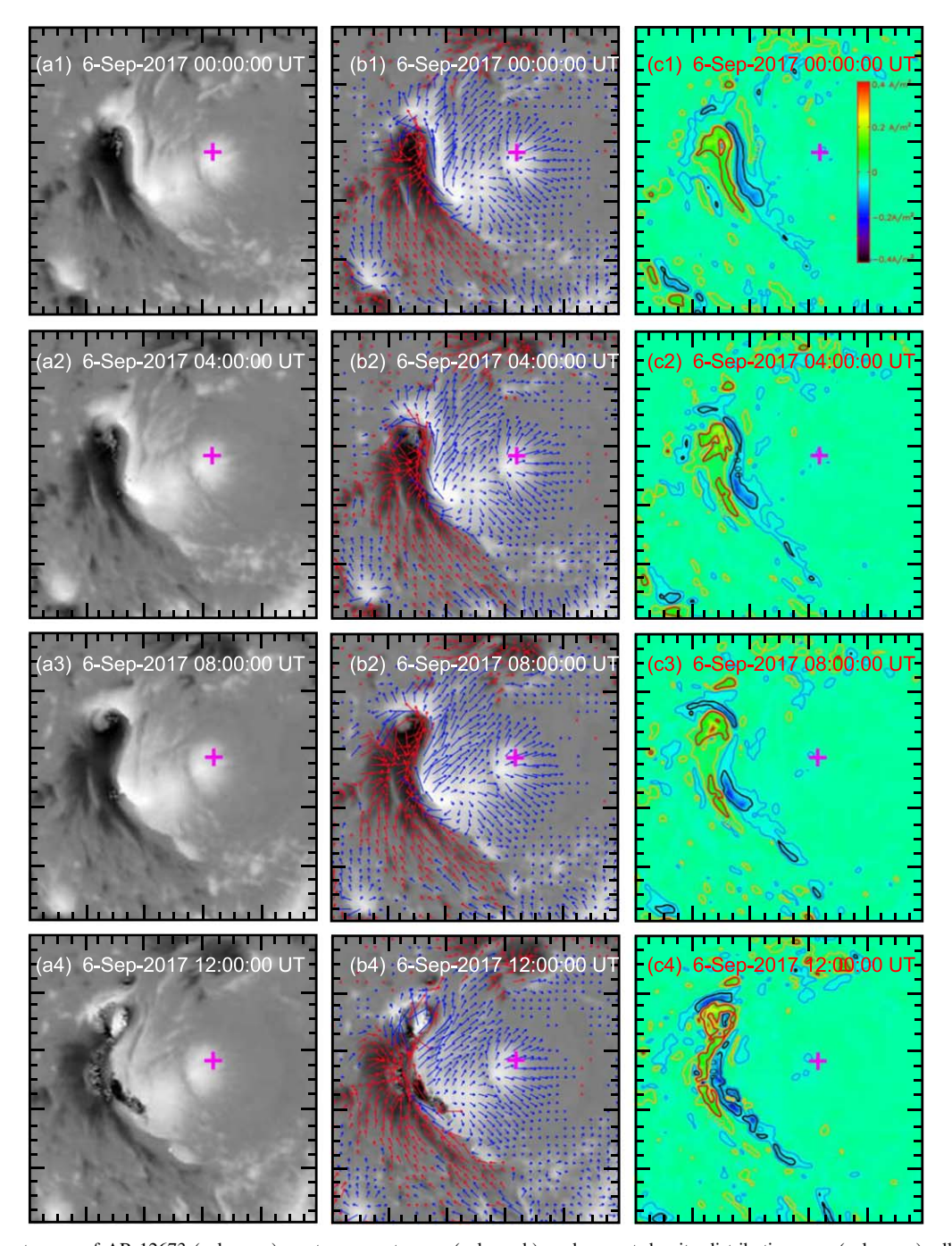


Figure 4. LOS magnetogram of AR 12673 (column a), vector magnetogram (column b), and current density distribution map (column c), all measured on 2017 September 6. The pink "+" symbol marks the center of the sunspot umbra.

Subsequently, the current density within the AR continued to evolve over time, exhibiting continuous changes. To understand the variation pattern of current density within the AR, we integrated the current density within the black square in Figure 5 to obtain the current intensity curve (as shown in Figure 7). The solid line represents the total intensity of positive currents within the AR, while the dashed line

represents the total intensity of negative currents within the AR. At 11:48 UT, just before the eruption of the X9.3-class flare, the current intensity rapidly increased. This increase in intensity is evidently closely related to the X9.3-class flare.

Based on the above two predicted positions, we observed the evolution of the solar flares. Figures 8 and 9 respectively show the eruption process of the X9.3-class flare in the 170 nm and

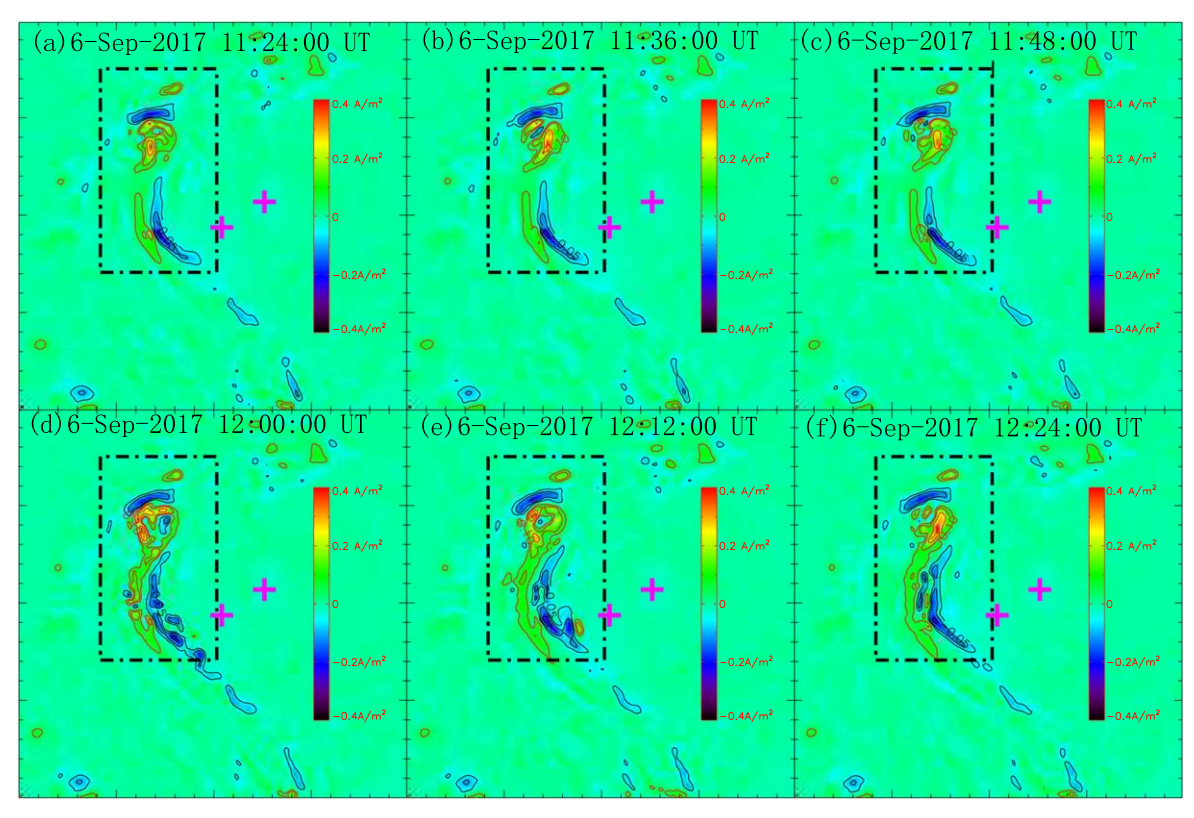


Figure 5. Current density distribution map of the AR on 2017 September 6. The pink "+" symbols indicate the positions of two sunspots, while the color bar on the right represents the current density.

30.4 nm images. All images are overlaid with white contours representing the current density of 60 mA m⁻² and the positions of the MNL are marked. The black squares correspond to the positions of the black squares in Figures 5 and 6. The flare began to brighten at 11:53:16 UT in the 170 nm image, appearing as a small bright core in the lower left corner of the square. This state lasted for about 1 minute. Five small bright cores appeared on the negative polarity current sheet at 11:54:04 UT. As time progressed, these small bright cores gradually formed a complete flare ribbon. Due to overexposure, the morphology of the flare in images after 11:55:16 UT could not be distinguished. It was not until 12:05:16 UT that the X9.3-class flare evolved into a doubleribbon flare located on both sides of the MNL. Similarly, the flare began to brighten in the form of a bright core at 11:55:05 UT in the 30.4 nm. The morphology of the flare continued to evolve over time. In the image at 12:00:55 UT, a distinct double-ribbon structure can be observed.

4. Conclusion and Discussion

Predicting future increases in solar activity well in advance undoubtedly holds significant societal importance (Raphaldini et al. 2023). Understanding space weather is becoming

increasingly important, as extreme solar eruptions may impact our daily activities, including the precision of global positioning systems (Abed et al. 2021). An effective forecasting system for solar activity should utilize high-quality data from real-time or near-real-time reliable sources and high-speed equipment for data processing (Gallagher et al. 2002). This work has become of great interest to many scientists for predicting solar flare eruptions (Lee et al. 2007; Park et al. 2018; Krista & Chih 2021). Under the high-quality SDO/HMI photospheric magnetic field vector measurements, we investigated some magnetic characteristics of the solar AR 12673 and their relationship with the X9.3-class major solar flare. We utilized the Ampère's Law integration algorithm to compute the current density distribution within the AR. This method effectively reduces the noise introduced during calculations, thereby increasing the reliability of the results.

Solar flare activity is closely related to changes in magnetic field topology, as eruptions of major flares can induce alterations in magnetic field topology. Research has shown that AR 12673 had dispersed current density distributions appearing as early as September 3, with continuous flare activity observed from that date, culminating in the X9.3-class flare eruption on September 6. Over time, new magnetic structures continued to emerge, and discrete currents gradually

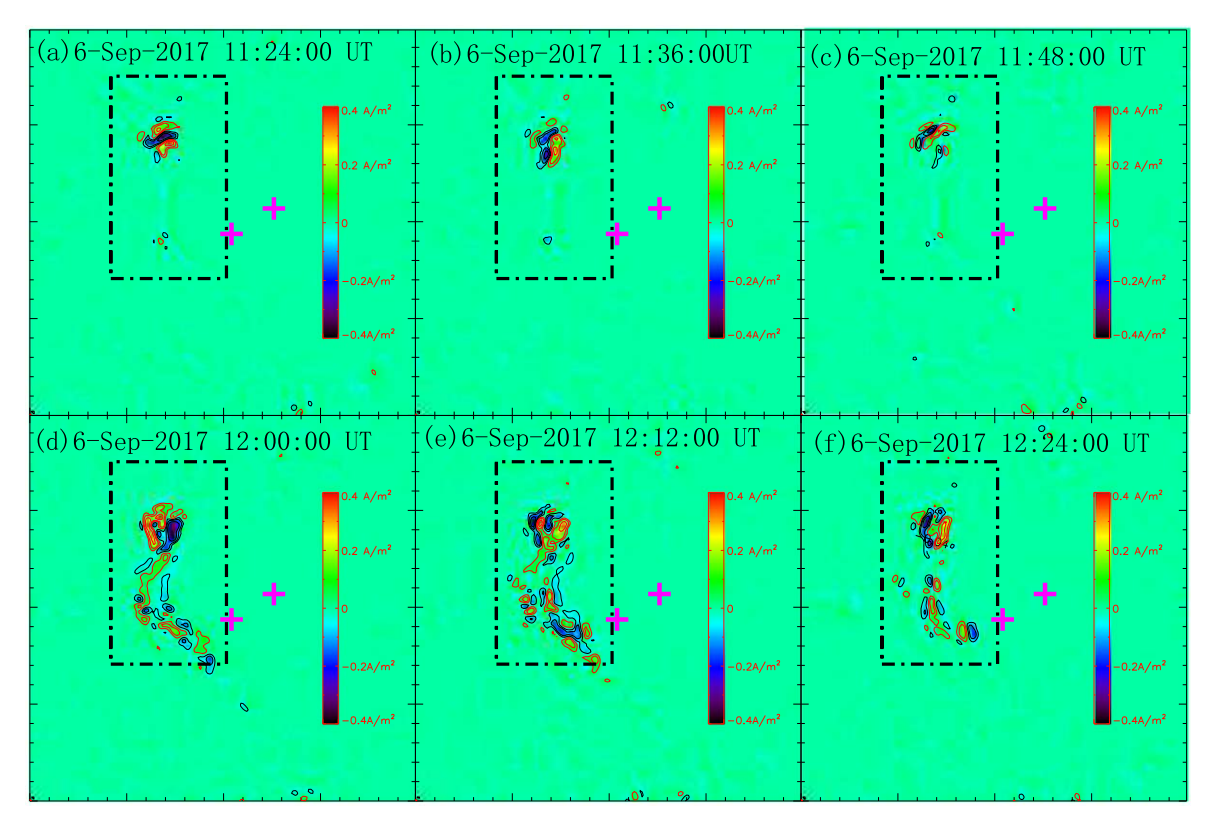


Figure 6. Current running-difference images of the AR from 11:24 to 12:24 UT on 2017 September 6. The pink "+" symbols indicate the positions of two sunspots, while the color bar on the right represents the current density.

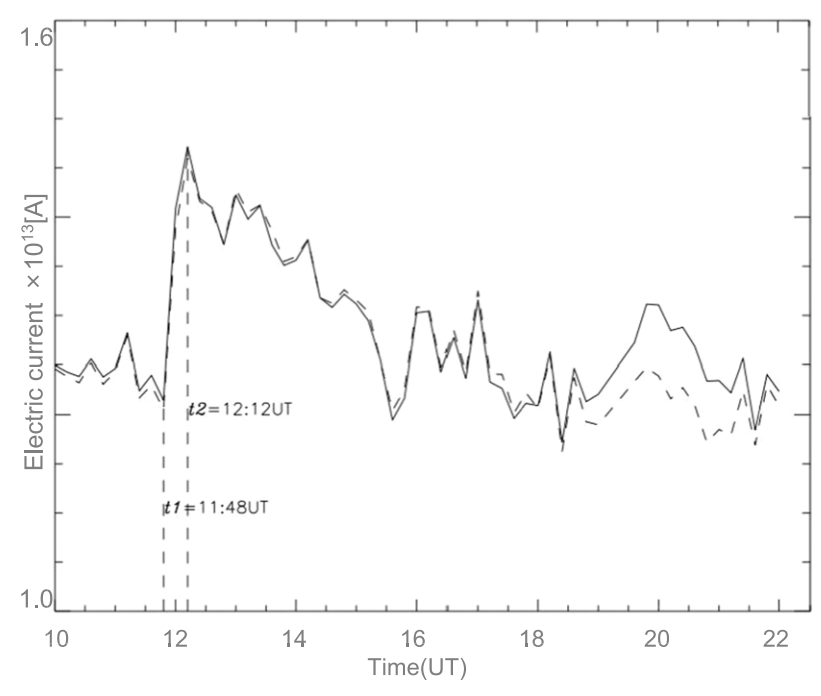


Figure 7. Integral Current Intensity Variation Chart for the AR from 10:00 to 22:00 UT on 2017 September 6. The horizontal axis represents time, and the vertical axis represents current intensity. Dashed lines indicate the intensity of negative pole currents, while solid lines indicate the intensity of positive pole currents.

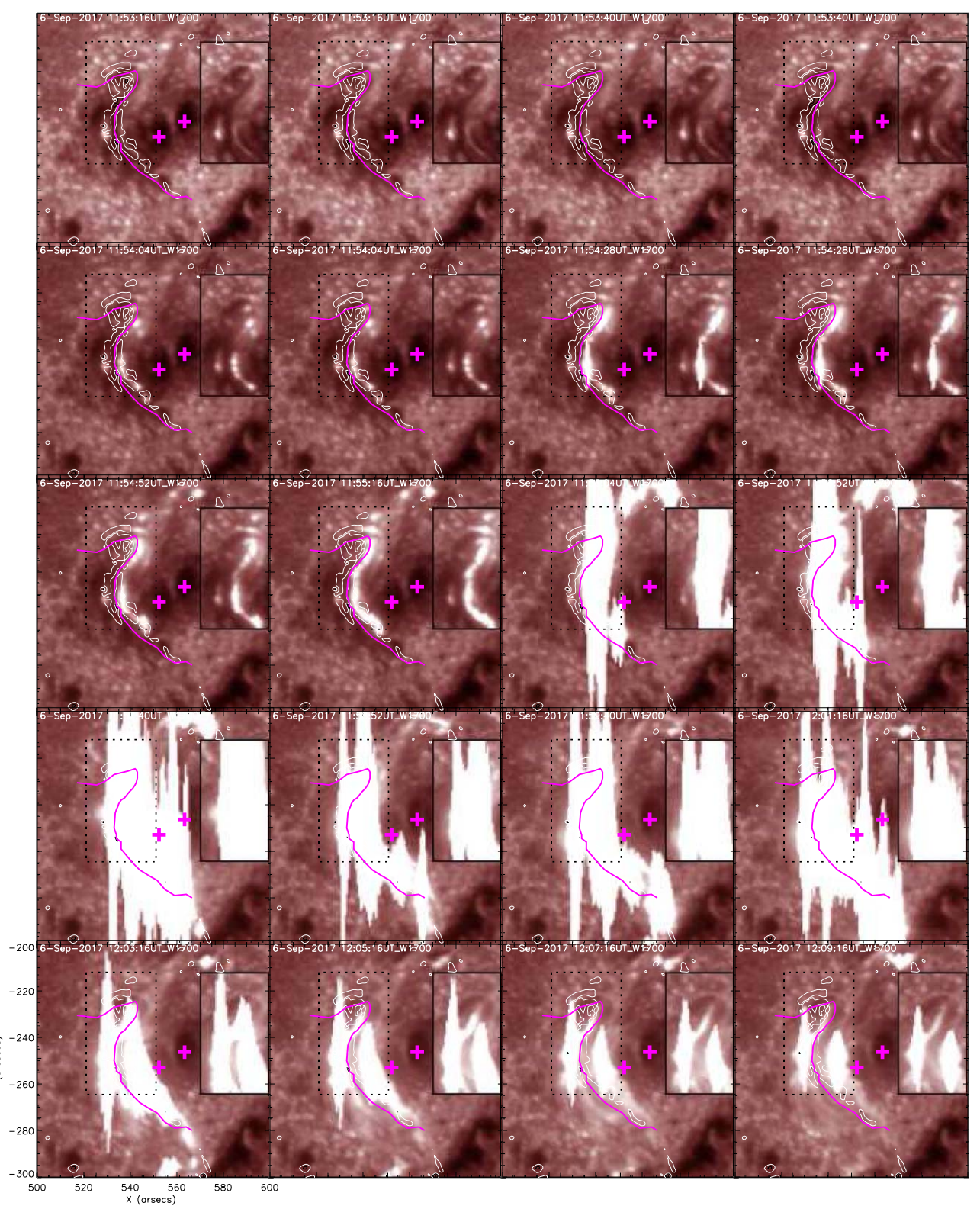


Figure 8. Eruptive process of the X9.3 flare acquired at 170 nm. All images have been overlaid with contour lines representing a current density value of 60 mA $\rm m^{-2}$, shown as white lines. The purple curve represents the MNL and the pink "+" symbols represent the positions of two sunspots. The black box outlines the main flare location.

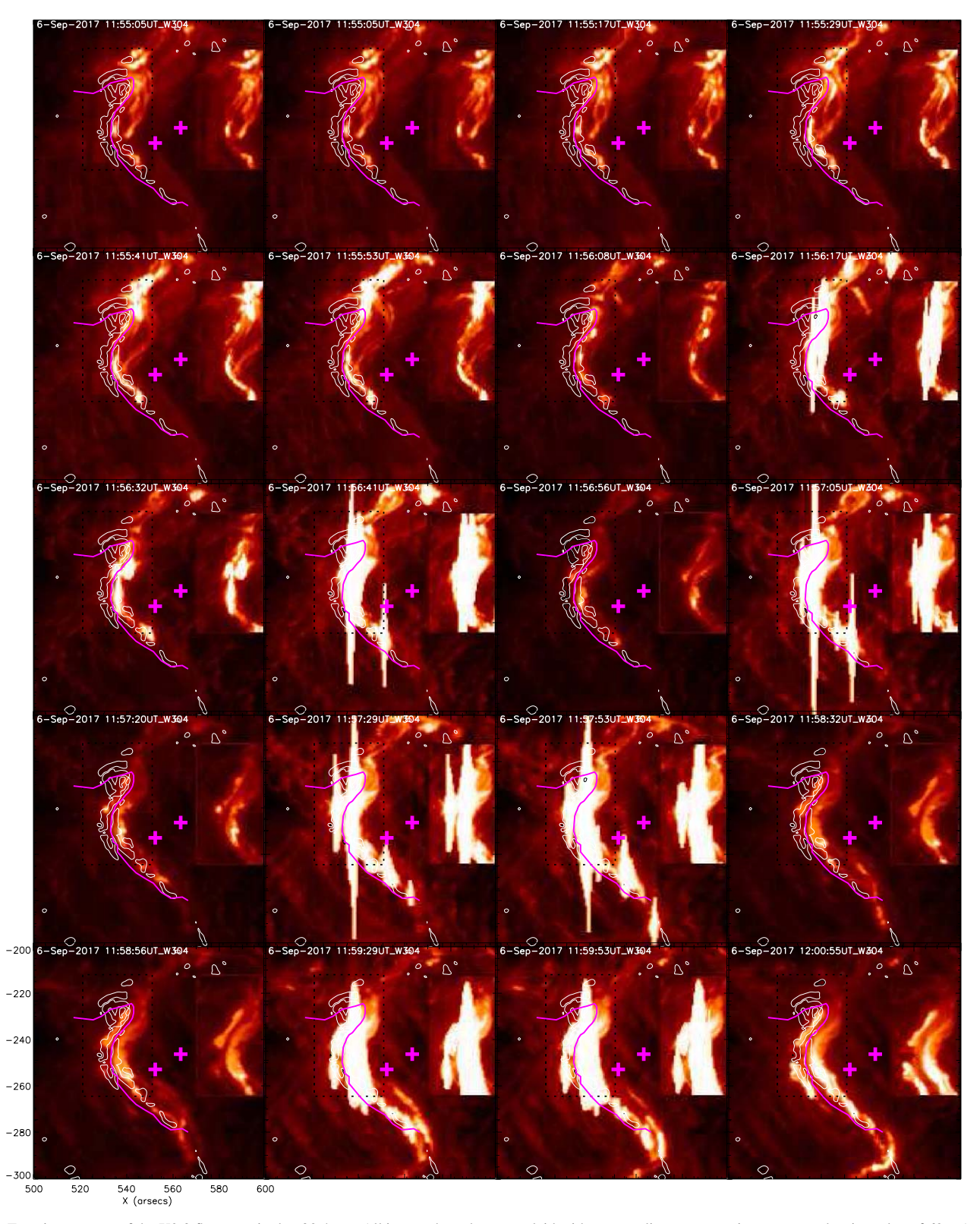


Figure 9. Eruptive process of the X9.3 flare acquired at 30.4 nm. All images have been overlaid with contour lines representing a current density value of 60 mA m^{-2} , shown as white lines. The purple curve represents the MNL and the pink "+" symbols represent the positions of two sunspots. The black box outlines the main flare location.

formed into an elongated pair of conjugate ribbons. In analyzing the evolution of solar flare morphology, we found that flares do not suddenly brighten but evolve gradually along the conjugate current ribbons with small bright cores, despite the rapid nature of this evolution. The final two-ribbon flare aligns closely in both form and position with the conjugate current ribbons. By calculating the distribution of current density within the active region, it helps us better understand the relationship between major solar flare eruptions and changes in current density characteristics.

It has been observed since the 1990s that the location of solar flare eruptions under higher current density can be predicted (Hagyard 1990). This study uses Ampère's law to calculate the evolution of current density during solar flare eruptions. Compared to previous findings (Janvier et al. 2014), our obtained current distribution is clearer. The high-resolution distribution of current density better illustrates the complexity of currents, robustly supporting the method of predicting solar flare eruption locations through higher current density calculations.

Acknowledgments

We would like to thank teams of SDO and GOES for providing the excellent data. This work is supported by the Natural Natural Science Foundation of China (NSFC, grant No. 12303062), Sichuan Science and Technology Program (2023NSFSC1351), Joint Funds of the National Natural Science Foundation of China (NSFC, grant No. U1931116), and the Project Supported by the Specialized Research Fund for State Key Laboratories. We also acknowledge the Sichuan Normal University Astrophysical Laboratory Supercomputer for providing the computational resources.

References

```
Abed, A. K., Qahwaji, R., & Abed, A. 2021, AdSpR, 67, 2544
Abramenko, V., Yurchishin, V., & Carbone, V. 1998, SoPh, 178, 35
Attié, R., Kirk, M. S., Thompson, B. J., Muglach, K., & Norton, A. A. 2018, SpWea, 16, 1143
```

```
Barnes, G., Leka, K., Schrijver, C., et al. 2016, ApJ, 829, 89
Berdermann, J., Kriegel, M., Banyś, D., et al. 2018, SpWea, 16, 1604
Borrero, J., Tomczyk, S., Kubo, M., et al. 2011, SoPh, 273, 267
Canfield, R. C., de La Beaujardiere, J.-F., Fan, Y., et al. 1993, ApJ, 411, 362
Chertok, I. M., Belov, A. V., & Abunin, A. A. 2018, SpWea, 16, 1549
Gallagher, P. T., Moon, Y.-J., & Wang, H. 2002, SoPh, 209, 171
Gosling, J., McComas, D., Phillips, J., & Bame, S. 1991, JGRA, 96, 7831
Hagyard, M. 1990, Società Astronomica Italiana, Memorie, 61, 337
Hou, Y. J., Zhang, J., Li, T., Yang, S. H., & Li, X. H. 2018, A&A, 619, A100
Janvier, M., Aulanier, G., Bommier, V., et al. 2014, ApJ, 788, 60
Jing, J., Park, S.-H., Liu, C., et al. 2012, ApJL, 752, L9
Krall, K., Smith, J., Hagyard, M., West, E., & Cummings, N. 1982, SoPh, 79, 59
Krista, L. D., & Chih, M. 2021, ApJ, 922, 218
Kusano, K., Iju, T., Bamba, Y., & Inoue, S. 2020, Sci, 369, 587
Lee, J., Moon, Y., Kim, K., Park, Y., & Fletcher, A. 2007, JKAS, 40, 99
Leka, K., Barnes, G., Crouch, A., et al. 2009, SoPh, 260, 83
Lin, Y. 2000, Introduction to Solar Physics (University of Chinese Academy of
  Sciences)
Lysenko, A. L., Anfinogentov, S. A., Svinkin, D. S., Frederiks, D. D., &
  Fleishman, G. D. 2019, ApJ, 877, 145
MacTaggart, D., Prior, C., Raphaldini, B., Romano, P., & Guglielmino, S. L.
  2021, NatCo, 12, 6621
Melrose, D. 1991, ApJ, 381, 306
Metcalf, T. R., Leka, K., & Mickey, D. 2005, ApJL, 623, L53
Mitra, P. K., Joshi, B., Prasad, A., Veronig, A. M., & Bhattacharyya, R. 2018,
Morosan, D. E., Carley, E. P., Hayes, L. A., et al. 2019, NatAs, 3, 452
Pariat, E., Démoulin, P., & Berger, M. A. 2005, A&A, 439, 1191
Park, E., Moon, Y.-J., Shin, S., et al. 2018, ApJ, 869, 91
Park, S.-H., Leka, K., Kusano, K., et al. 2020, ApJ, 890, 124
Pesnell, W. D., Thompson, B. J., & Chamberlin, P. C. 2012, Sol. Phys., 275, 3
Raboonik, A., Safari, H., Alipour, N., & Wheatland, M. S. 2016, ApJ, 834, 11
Raphaldini, B., Dikpati, M., Norton, A. A., et al. 2023, ApJ, 958, 175
Ravindra, B., Venkatakrishnan, P., Tiwari, S. K., & Bhattacharyya, R. 2011,
   ApJ, 740, 19
Redmon, R. J., Seaton, D. B., Steenburgh, R., He, J., & Rodriguez, J. V. 2018,
  pWea, 16, 1190
Regnier, S., & Priest, E. 2007, ApJ, 669, L53
Savage, S. L., McKenzie, D. E., Reeves, K. K., Forbes, T. G., &
  Longcope, D. W. 2010, ApJ, 722, 329
Scolini, C., Chané, E., Temmer, M., et al. 2020, ApJS, 247, 21
Simpson, J. J. 2011, JGR, 116, A11
Vanselow, K. H. 2020, JAsB, 19, 413
Vasantharaju, N., Vemareddy, P., Ravindra, B., & Doddamani, V. H. 2019,
   ApJ, 874, 182
Wang, H., Ewell, M., Jr, Zirin, H., & Ai, G. 1994, ApJ, 424, 436
Welsch, B. T., Fisher, G. H., & Sun, X. 2013, ApJ, 765, 98
Wilkinson, L. K., Emslie, A., & Gary, G. 1992, ApJL, 392, L39
Yamasaki, D., Inoue, S., Nagata, S., & Ichimoto, K. 2021, ApJ, 908, 132
Yang, S., Zhang, J., Zhu, X., & Song, Q. 2017, ApJL, 849, L21
```